Check for updates

Geophysical Research Letters

RESEARCH LETTER
10.1029/2025GL117992

Quantifying the Relationships Between Dynamics and Rainfall Intensity Along the Mei-Yu Front During PRECIP 2022

Jennifer C. DeHart[1] **and Michael M. Bell**[1]

[1]Colorado State University, Fort Collins, CO, USA

Key Points:

- Prediction of Rainfall Extremes Campaign in the Pacific 2022 analyses show the highest rain totals in oceanic Mei-Yu fronts preferentially occur in moderately strong rotating convection
- Five hundred forty-five Multi-Doppler analyses show increases in relative vorticity, vertical velocity, and low-level convergence with rain rate intensity
- Forty-five percent of the volumetric rain accumulation comes from rain rates between 10 and 50 mm h^{-1} that comprise only 6% of the raining grid points

Supporting Information:

Supporting Information may be found in the online version of this article.

Correspondence to:

J. C. DeHart,
jcdehart@colostate.edu

Citation:

DeHart, J. C., & Bell, M. M. (2025). Quantifying the relationships between dynamics and rainfall intensity along the Mei-Yu front during PRECIP 2022. *Geophysical Research Letters*, *52*, e2025GL117992. https://doi.org/10.1029/2025GL117992

Received 3 JUL 2025
Accepted 27 NOV 2025

Author Contributions:

Conceptualization: Jennifer C. DeHart, Michael M. Bell
Formal analysis: Jennifer C. DeHart, Michael M. Bell
Funding acquisition: Michael M. Bell
Methodology: Jennifer C. DeHart, Michael M. Bell
Project administration: Michael M. Bell
Supervision: Michael M. Bell
Writing – original draft: Jennifer C. DeHart
Writing – review & editing: Jennifer C. DeHart, Michael M. Bell

© 2025 The Author(s).
This is an open access article under the terms of the Creative Commons Attribution-NonCommercial License, which permits use, distribution and reproduction in any medium, provided the original work is properly cited and is not used for commercial purposes.

Abstract Multi-Doppler analyses from the joint Prediction of Rainfall Extremes Campaign in the Pacific 2022 and Taiwan-Area Heavy rain Observation and Prediction Experiment field campaign are used to examine the relationships between dynamics and rainfall intensity in two Mei-Yu frontal periods. Statistics from oceanic rainfall over 8 days show a mean increase and a positive shift of the distributions of vertical vorticity, vertical motion, and divergence with increasing rain rate intensity. In regions of higher rain rates, mean ascent maximizes in the upper troposphere, low-level convergence intensifies over a deeper layer, and upper-level divergence strengthens. Stratiform rainfall is frequent in light rain rates below 5 mm h^{-1} but contributes little to the total rainfall. Heavy convective rain rates between 10 and 50 mm h^{-1} are only 6% of the observed raining grid points over the ocean but contribute over 45% of the total volumetric rainfall. The radar analysis indicates that the highest rain accumulations in the oceanic Mei-Yu precipitation preferentially occur in moderately strong rotating convection.

Plain Language Summary Heavy rainfall is a result of complex circulation and interactions between cloud droplets, raindrops, snow, and ice. Doppler radar observations from the Prediction of Rainfall Extremes Campaign in the Pacific/Taiwan-Area Heavy rain Observation and Prediction Experiment field campaign are analyzed to provide three-dimensional wind fields to study the physical mechanisms that produce heavy rain within two Mei-Yu frontal periods. These analyses show that regions of heavy rainfall over the ocean were more likely to have rotating clouds than regions with lighter rainfall. These rotating clouds with high rain rates were found in only about 6% of the observed locations where it was raining but produced 45% of the rainfall. The results from this research help identify the most important regions and mechanisms that produce heavy rainfall and can help focus future efforts to improve rainfall prediction.

1. Introduction

Heavy rainfall that can lead to flooding remains one of the most damaging weather phenomena around the world. The ingredients that produce heavy rain are known (Doswell et al., 1996), but rainfall prediction remains challenging in part due to multi-scale interactions that can focus these ingredients into localized regions of extreme rain rates. One particular example of this challenge is prediction of heavy rain associated with the Mei-Yu front in the moisture-rich East Asian Summer Monsoon. On the synoptic scale, the Mei-Yu front represents a boundary between warm, moist southwesterly flow and relatively cooler, drier air to the north. The heaviest rain falls from mesoscale convective systems (MCSs) that move eastward along the front (G. T.-J. Chen, 1983; Ninomiya & Murakami, 1987; Tao & Chen, 1987; Xu et al., 2009). Mei-Yu frontal precipitation forecasts require accurate representation of the many different scales, including the synoptic-scale front, synoptically- and topographically-forced horizontal jets, MCSs within the frontal zone, and microphysical processes (Y.-L. Chen et al., 2022; Chien & Chiu, 2023; Wang et al., 2021). Our fundamental understanding and predictability of mesoscale phenomena within the Mei-Yu front is still limited (Paul et al., 2018; Wang et al., 2021, 2022). To address these limitations, the National Science Foundation (NSF)-supported Prediction of Rainfall Extremes Campaign in the Pacific (PRECIP) experiment was conducted in 2022 in Taiwan and southern Japan with the goal of improving our understanding of the fundamental causes of extreme rainfall, including within the Mei-Yu front.

Prior statistical studies of profiler measurements of vertical motion in general tropical convection show ascent maximizing in the upper troposphere that is more intense within heavier rainfall compared to lighter rainfall (Balsley et al., 1988; W.-Y. Chang et al., 2015; Cifelli & Rutledge, 1998; Schumacher et al., 2015). Prior Dual-Doppler analysis has demonstrated the importance of low- and mid-level convergence, low-level vertical wind

19448007, 2025, 24, Downloaded from https://agupubs.onlinelibrary.wiley.com/doi/10.1029/2025GL117992, Wiley Online Library on [06/02/2026]. See the Terms and Conditions (https://onlinelibrary.wiley.com/terms-and-conditions) on Wiley Online Library for rules of use; OA articles are governed by the applicable Creative Commons License

shear, and cold pools to the evolution of convection within the Mei-Yu front (e.g., Ke et al., 2019; Zhou, 2009). W.-Y. Chang et al. (2015) analyzed 2 days worth of dual-Doppler retrievals within a pre-frontal airmass southwest of Taiwan and showed slight differences in both the height of maximum ascent and intensity and depth of low-level convergence between different convective types, but they did not examine how the kinematic and dynamic variables scaled with rainfall intensity.

Recent work has also shown positive relationships between vertical vorticity and rainfall. Numerical simulations from Coffer and Parker (2015) and Nielsen and Schumacher (2018) showed that the forcing from pressure perturbations within strong rotation was capable of enhancing ascent and rainfall locally similar to the lifting mechanism found in continental supercells (Klemp, 1987; Rotunno & Klemp, 1982). In tropical environments, frictional boundary layer convergence (Eliassen & Lystad, 1977) and isentropic uplift ahead of PV anomalies in sheared flow (Deng et al., 2017; Lai et al., 2011; Raymond & Jiang, 1990; Trier et al., 2000) are mechanisms that can produce ascent in rotating flow. Mazurek and Schumacher (2023) found a positive relationship between a rotation proxy and radar-derived rain rates in observations of a landfalling tropical storm. Convective updrafts can also enhance rotation through vortex stretching, potentially resulting in positive feedbacks that further enhance rainfall.

We focus in this study on the relationship between rainfall intensity and the dynamic quantities of vertical vorticity, vertical velocity, and divergence using the field observations collected during PRECIP 2022. The NSF National Center for Atmospheric Research (NCAR) S-Pol radar was deployed in northwestern Taiwan during PRECIP for 78 days in collaboration with the Taiwan-Area Heavy rain Observation and Prediction Experiment (TAHOPE) and Japanese Tropical cyclones-Pacific Asian Research Campaign for Improvement of Intensity estimations/forecasts (T-PARCII) field campaigns. By combining with nearby operational and research radars, the field observations provide an opportunity for multi-Doppler analysis over a larger domain and longer time period than prior studies.

We hypothesize that in a moisture-rich environment higher rainfall rates are due primarily to increases in organized dynamically-forced ascent that are not from fundamentally different processes than lower rain rates. To test this hypothesis we analyze data from two intensive operating periods (IOPs) that observed Mei-Yu frontal precipitation on 26–28 May and 6–12 June 2022. Doppler and polarimetric radar data provide coincident mesoscale observations of dynamic variables and rainfall that enable statistical analysis to test the above hypothesis. Section 2 provides a brief description of the data and multi-Doppler analysis methodology. Additional technical details are provided in Supporting Information S1. Key results from the analysis are presented in Section 3. A summary of the main conclusions is provided in the final section.

2. Data and Methodology

Taiwan has a dense operational Doppler radar network (P.-L. Chang et al., 2021). During PRECIP, the addition of S-Pol expanded the potential multi-Doppler coverage (Figure 1a). S-Pol is a 2.81 GHz (S band) radar, which operated nearly continuously over the campaign (NCAR/EOL S-Pol Team, 2024). A 12-min repeated scan strategy with a volume scan consisting of 10 elevation angles (0.5–11°) provided the necessary spatial coverage for multi-Doppler analysis and quantitative precipitation estimation. The multi-Doppler analysis also used the Taiwan Experimental Atmospheric Mobile Radar (TEAM-R) X-band radar from National Central University (NCU) as part of TAHOPE and four operational Taiwan Central Weather Administration (CWA) radars: RCWF, RCTP, RCSL, and RCNT. RCWF is an S-band radar and RCTP, RCSL, and RCNT are C-band radars. All except RCTP are polarimetric radars.

S-Pol data underwent an initial engineering quality control by EOL staff at NSF NCAR to correct measurement biases and remove obvious noise (NCAR/EOL S-Pol Team, 2024). Remaining non-meteorological echoes, noise, and points contaminated by terrain blockage were removed using polarimetric variable thresholds, the NSF NCAR fuzzy logic particle identification algorithm in the Lidar Radar Open Software Environment's (LROSE) RadxPid, and Py-ART's velocity texture algorithm (DeHart et al., 2024; Helmus & Collis, 2016; Vivekanandan et al., 1999). Details regarding the echo and noise quality control can be found in Text S1 in Supporting Information S1.

The maximum Nyquist velocity of RCTP was only 16.77 m s^{-1} and required dealiasing, but the other five radars had Nyquist velocities over 28 m s^{-1} such that velocity aliasing is infrequent in the data set. Py-ART's region-

10.1029/2025GL117992

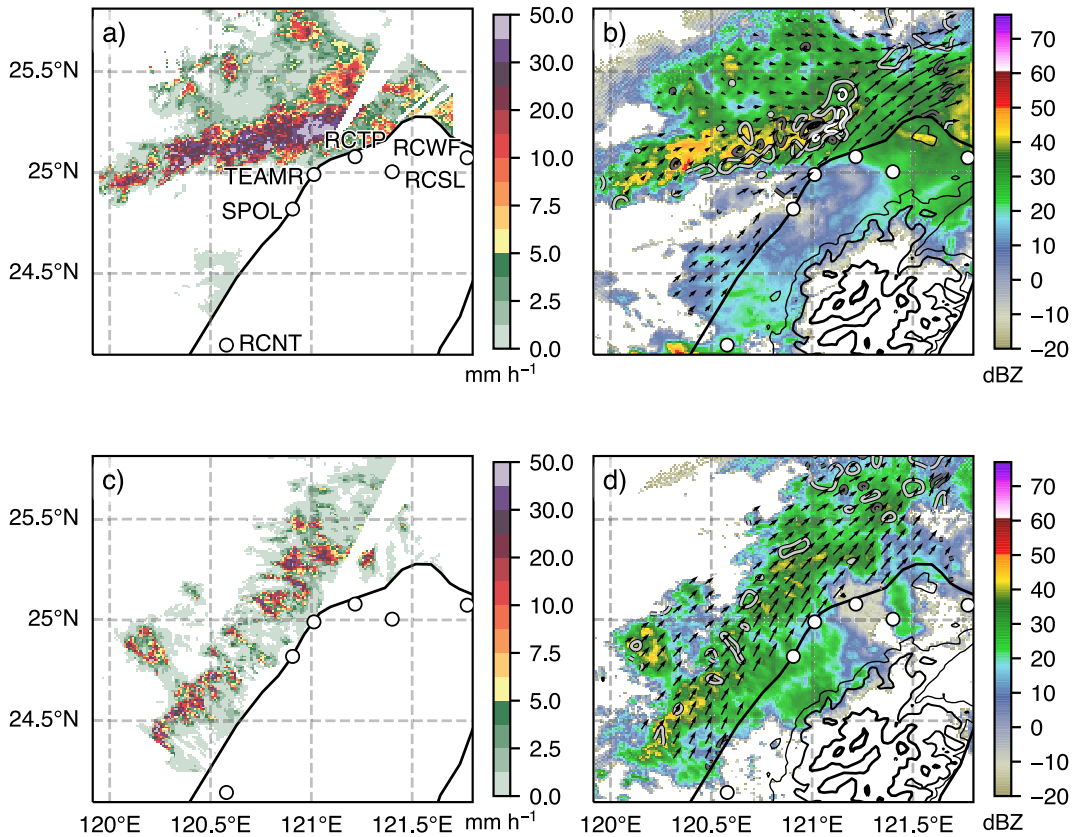

Figure 1. (a) Map of estimated rain rate from S-Pol (mm h^{-1}) and radar locations at 07:13 UTC 6 June 2022. (b) As in (a), but of SAMURAI analyzed reflectivity (shading), horizontal winds (vectors, m s^{-1}), and vorticity (outlined contours where white colors indicate positive values, −200, −75, 75, 200 10^{-5} s^{-1}) at 1.5-km altitude. Black contours of increasing thickness indicate terrain (0.5, 1, 2, and 3 km). (c, d) As in (a, b), but at 02:49 UTC 26 May 2022.

based unfolding algorithm and NSF NCAR's solo3 software were used to dealias the RCTP velocity data (Helmus & Collis, 2016; Oye et al., 1995). RCNT uses dual-pulse repetition frequencies to extend the Nyquist velocity; processing errors in turbulent regions were corrected using the processorCorrect Python package (Alford et al., 2022). Details regarding the velocity correction procedures can be found in Text S2 in Supporting Information S1.

Once the data were quality controlled, three-dimensional multi-Doppler analyses were created using SAMURAI (Bell et al., 2012), which is a variational global solver that implements immersed boundary conditions to produce analyses over complex terrain (Cha & Bell, 2023). Each SAMURAI analysis was anchored on S-Pol's surveillance scans during the Mei-Yu IOPs (26–28 May and 6–12 June 2022). To reduce temporal aliasing, surveillance scans from all 6 radars were required to start within 8 min of the start of S-Pol's surveillance scan. In total, 545 analyses met these criteria. The horizontal and vertical grid spacings were 1 and 0.5 km, respectively. To reduce noise and prevent overfitting, Gaussian spatial filters were applied, which reduce the effective horizontal resolution to the meso-γ scale (~4 km). Details regarding the SAMURAI analyses can be found in Text S3 in Supporting Information S1.

Rain rates were estimated using the NSF NCAR hybrid algorithm and gridded to the SAMURAI domain using LROSE's RadxRate and Radx2Grid, respectively (DeHart et al., 2024; Dixon et al., 2015). To maximize data coverage, the rain rates at 1.5-km altitude were used as representative of the near surface rain rates. While there were likely variations in the rain rate from 1.5 km to the surface, the use of a fixed altitude allows for a consistent relative comparison with the multi-Doppler analyses. The Echo Classification from COnvectivity (ECCO) classifier (Dixon & Romatschke, 2022) was used for convective-stratiform partitioning. ECCO evaluates reflectivity using a scale of convectivity, where a third "mixed" category is a buffer zone that often surrounds

19448007, 2025, 24, Downloaded from https://agupubs.onlinelibrary.wiley.com/doi/10.1029/2025GL117992, Wiley Online Library on [06/02/2026]. See the Terms and Conditions (https://onlinelibrary.wiley.com/terms-and-conditions) on Wiley Online Library for rules of use; OA articles are governed by the applicable Creative Commons License

19448007, 2025, 24, Downloaded from https://agupubs.onlinelibrary.wiley.com/doi/10.1029/2025GL117992, Wiley Online Library on [06/02/2026]. See the Terms and Conditions (https://onlinelibrary.wiley.com/terms-and-conditions) on Wiley Online Library for rules of use; OA articles are governed by the applicable Creative Commons License

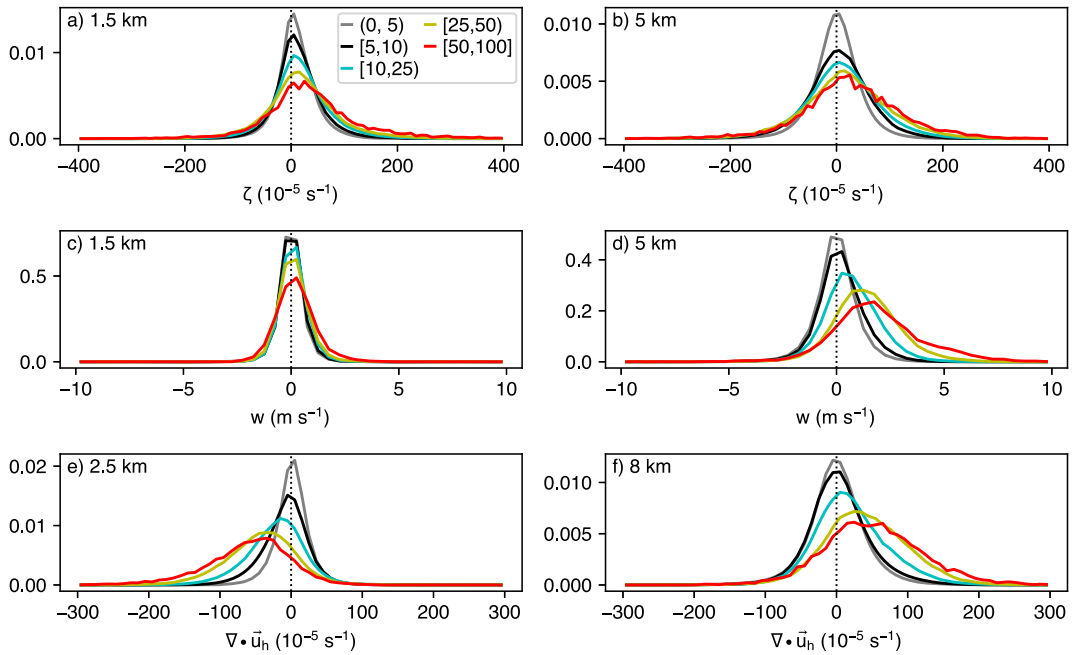

Figure 2. (a) Normalized probability distributions of vertical vorticity (10^{-5} s^{-1}) for rain rates between 0 and 5, 5 and 10, 10 and 25, 25 and 50, and 50 and 100 mm h^{-1} at 1.5-km altitude. (b) As in (a), but at 5 km. (c, d) As in (a, b), but for vertical velocity (m s^{-1}). (e, f) As in (a, b), but for divergence (10^{-5} s^{-1}) at 2.5 and 8 km.

convective pixels. ECCO subdivides convective and stratiform precipitation by echo height, but we aggregate all subcategories into the three primary precipitation types. Details regarding the echo analysis can be found in Text S4 in Supporting Information S1.

Though winds and polarimetry were available over the mountains of Taiwan, only oceanic data were examined in this study to simplify the problem and focus on dynamically produced ascent within the Mei-Yu front rather than orographic lifting (Figures 1a and 1c). An additional simplification is that all comparisons occur within vertical columns, with no attempt to account for slantwise convection. Non-local rain production and orographic effects will be considered in future work.

3. Results

3.1. Statistical Relationships Between Dynamic Variables and Rain Rates

Two examples of the rain rate and low-level kinematic fields are shown in Figure 1; heavy rain is often, but not always associated with stronger cyclonic vorticity. Figure 2 shows normalized probability distributions of relative vertical vorticity, vertical velocity, and divergence for different rain rates in the low and mid troposphere. The distributions are normalized such that the integral along each curve equals 1 to compare across the vastly different sample sizes in each rain rate bin. The distributions of vorticity at both 1.5- and 5-km altitude (Figures 2a and 2b) are narrow and symmetric for the weakest rain rates. As the rain rate increases, the vorticity distributions broaden, the modes shift to more positive vorticity, and stronger, positive vorticity is more frequent. The increase in the positive tail of the vorticity distributions is more apparent at 5-km altitude than at 1.5-km altitude.

The increased likelihood for stronger rotation at higher rain rates is consistent with the results from Mazurek and Schumacher (2023) in a tropical storm. Our distributions indicate that the strongest vorticity values from the Mei-Yu cases are on the order of $10^{-3}s^{-1}$ on the 1-km SAMURAI grid, which includes an approximately 4-km low-pass filter. The horizontal grid spacings for the simulations analyzed by Coffer and Parker (2015) and Nielsen and Schumacher (2018) are lower (0.25 and 0.5 km, respectively) and their simulated relative vorticity magnitudes are orders of magnitude larger than the relative vorticity values seen in Figures 2a and 2b. Neither of those studies shows the full statistics of the simulated storms, but Nielsen and Schumacher (2018) shows that low-level vorticity values surpassing $10^{-3}s^{-1}$ are not uncommon and the maximum values routinely surpass $10^{-2}s^{-1}$. In

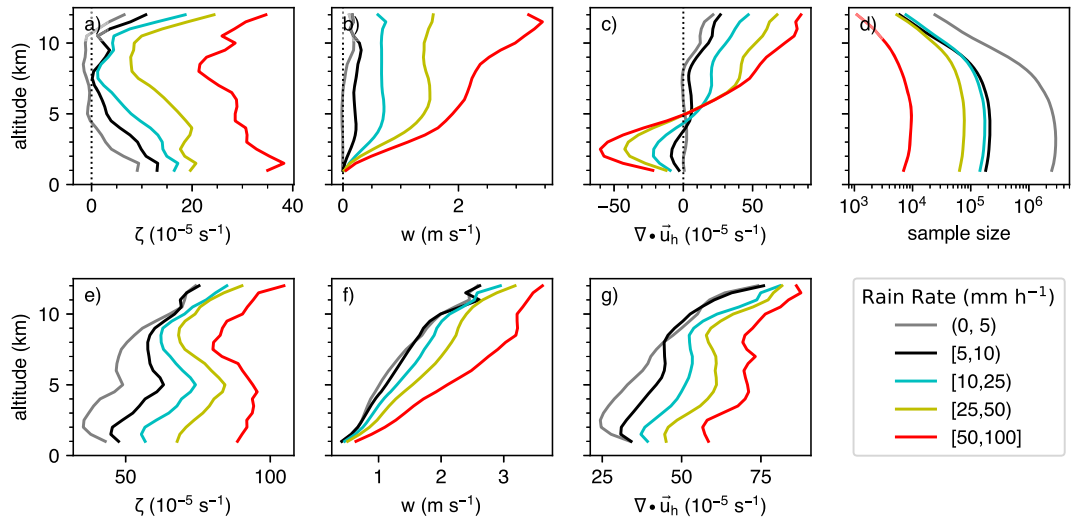

Figure 3. (a) Vertical profiles of mean vertical vorticity (10^{-5} s^{-1}) for rain rates between 0 and 5, 5 and 10, 10 and 25, 25 and 50, and 50 and 100 mm h^{-1}. (b) As in (a), but of vertical velocity (m s^{-1}). (c) As in (a), but of divergence (10^{-5} s^{-1}). (d) As in (a), but of sample size. (e–g) As in (a–c), but of standard deviation.

Coffer and Parker (2015), the maximum vorticity values often exceed $10^{-2}s^{-1}$ and peak above $10^{-1}s^{-1}$. Despite these differences in magnitude, the observational evidence shown here provide complementary evidence that higher rain rates are associated with stronger rotation in the subtropical Mei-Yu front environment.

The vertical velocity (w, Figures 2c and 2d) and divergence (Figures 2e and 2f) distributions also shift systematically with increasing rain rate intensity. Similar to vorticity, the w distributions are less peaked and exhibit larger spread for stronger rain rates. There is a stronger dependence on altitude than vorticity, with a mid-level increase to stronger ascent for the strongest rain rates (Figure 2d), consistent with prior studies (Balsley et al., 1988). Both the mean and variance of w increase within the strongest rain rates. The majority of the meso-γ w values are less than 5 m s^{-1} for all rain rates. The results suggest that heavy rain can be produced in this moist environment with moderate mesoscale ascent, but we acknowledge that stronger convective scale ascent may also play an important role. Stronger convective updrafts may have contributed to the observed rainfall rates due to the physical time lag in precipitation development as well as the spatial and temporal smoothing in the multi-Doppler analysis (e.g., Marinescu et al. (2020)).

Consistent with the increasing ascent, low-level convergence and upper-level divergence also strengthen as rain rate intensities increase, particularly for rain rates above 10 mm h^{-1} (Figures 2e and 2f). The change in divergence distributions with rain rate indicate increasingly strong secondary circulations, consistent with the w distribution and prior surface station results (Ulanski & Garstang, 1978). The distributions of w and divergence provide quantitative observational evidence of the known physical relationships between rainfall production and moist convective ascent. We acknowledge that the w and divergence are linked in the multi-Doppler analysis via a mass continuity constraint, but the rain rates are calculated independently from the polarimetric information. The results show quantitative evidence that higher rain rates are associated with progressively stronger dynamic forcing.

The mean, standard deviation, and sample size of the dynamic variables as a function of height are shown in Figure 3. The mean vorticity increases with rain rate intensity at all altitudes (Figure 3a). Mean vorticity maximizes near the surface and decreases to a minimum value around 8-km altitude before increasing again above 10 km. The upper-level vorticity maxima are likely related to reduced sample size aloft (Figure 3d). SAMURAI only returns kinematic data where there is sufficient echo, so the upper-level averages are likely skewed toward stronger and deeper convection.

Mean ascent increases with both rain rate intensity and altitude (Figure 3b), consistent with observed deep convective vertical velocity profiles in tropical convection (Balsley et al., 1988; Cifelli & Rutledge, 1998; Houze, 1989; Schumacher et al., 2015). The increase in ascent slows above the melting level for most profiles except the most intense rainfall; the height where w transitions to a near-constant value with height in the weaker

19448007, 2025, 24, Downloaded from https://agupubs.onlinelibrary.wiley.com/doi/10.1029/2025GL117992, Wiley Online Library on [06/02/2026]. See the Terms and Conditions (https://onlinelibrary.wiley.com/terms-and-conditions) on Wiley Online Library for rules of use; OA articles are governed by the applicable Creative Commons License

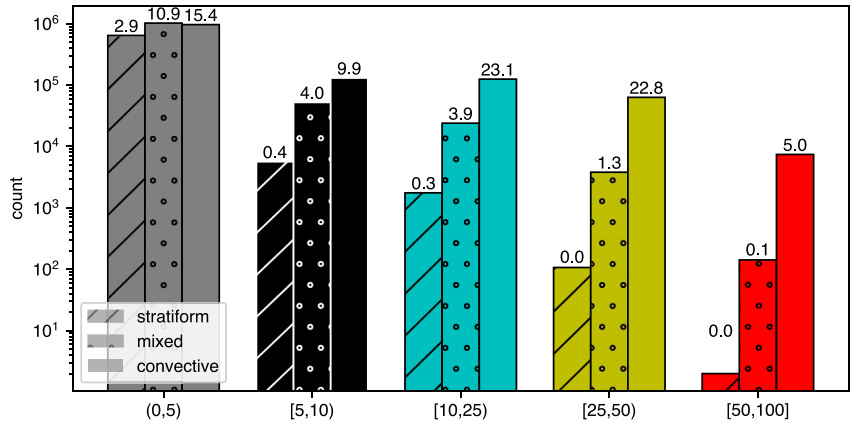

Figure 4. Frequencies of convective, stratiform, and mixed precipitation for each rain rate intensity bin. Numbers above each bar indicate the percentage contribution to the total volumetric rain.

rain rates is consistent with the behavior of the weaker-rain profile found by Balsley et al. (1988), although the transition happens at a lower altitude and the mean velocity in our data set is stronger. The upper-level increase in ascent is also similar to the deep convective profiles of *w* observed by Schumacher et al. (2015) and W.-Y. Chang et al. (2015). Notably, the mean vertical velocity values above 10-km altitude in our analysis do not trend toward 0 as they do in the convective profiles from W.-Y. Chang et al. (2015). This discrepancy could be a result of the different multi-Doppler techniques, averaging over all convective pixels smoothing out the strongest ascent, or different underlying convective populations. Nonetheless, the heaviest rainfall is associated with deeper, more intense convection. The inflection point where the increase in ascent begins to slow lies just below the altitudes where vorticity begins to decrease, suggestive of stretching within convection.

The divergence profiles transition from low-level convergence to upper-level divergence consistent with convective mass flux. The peak magnitudes of low-level convergence and upper-level divergence increase with rain rate intensity (Figure 3c). There is a slight increase in the altitude of the peak low-level convergence from 2 to 2.5 km from the 5–10 mm h^{-1} to the 50–100 mm h^{-1} rain rates, which could reflect a deeper layer of convergence in the heaviest rain. W.-Y. Chang et al. (2015) found convection in their squall line case also had a deeper layer of convergence, while the pre-frontal MCSs had larger maximum values. Separating by rain intensity in the current analysis shows that both deeper and larger maximum convergence are found for the strongest rain rates. In the lowest rain rate intensity bin, there is very slight divergence around 3-km altitude and convergence around 7-km altitude, indicative of a greater occurrence of stratiform precipitation compared to the other rain rate bins. Separating the vertical *w* profile for the weakest rain rate bin into convective and stratiform profiles reveals opposite vertical profiles of divergence (not shown).

The standard deviations of vorticity, *w*, and divergence increase with rain rate intensity and altitude (Figures 3e–3g). While there is substantial overlap in the distributions due to the spread, the different distribution shapes in Figure 2 and the systematic, gradual way in which they change with rain rate intensity are believed to be physically meaningful. The concurrent increase in the magnitudes of the mean and standard deviation indicate that higher values of these three dynamic variables are more likely with higher rain rates.

3.2. Convective Stratiform Partitioning

To confirm the dynamic results in terms of the role of deep convection, we examine the nature of the precipitation by categorizing each column as convective, stratiform, or mixed precipitation using ECCO (Dixon & Romatschke, 2022). In the PRECIP Mei-Yu IOPs, the relative frequency of convective precipitation increases as rain rates increase (Figure 4). For the highest rain rates, there are 3 orders of magnitude more convection than stratiform precipitation. Even in the 5–10 mm h^{-1} bin, there is over an order of magnitude more convection than stratiform. The lowest rain rate intensity has an even split between convective, mixed, and stratiform precipitation. Splitting Figures 2 and 3 by precipitation type reflects the dominance of convective points above 5 mm h^{-1}. The biggest changes occur below 5 mm h^{-1}, where convective points exhibit weak ascent, low-level cyclonic

19448007, 2025, 24, Downloaded from https://agupubs.onlinelibrary.wiley.com/doi/10.1029/2025GL117992, Wiley Online Library on [06/02/2026]. See the Terms and Conditions (https://onlinelibrary.wiley.com/terms-and-conditions) on Wiley Online Library for rules of use; OA articles are governed by the applicable Creative Commons License

19448007, 2025, 24, Downloaded from https://agupubs.onlinelibrary.wiley.com/doi/10.1029/2025GL117992, Wiley Online Library on [06/02/2026]. See the Terms and Conditions (https://onlinelibrary.wiley.com/terms-and-conditions) on Wiley Online Library for rules of use; OA articles are governed by the applicable Creative Commons License

vorticity and convergence, and upper-level divergence, while mixed and stratiform points exhibit canonical stratiform structures of low- to mid-level descent, low-level divergence, and upper-level convergence (not shown).

The highest rain rates have a relatively small contribution to the total volumetric rainfall. Although the rain rates are extreme, they are infrequent and contribute only 5% of the total rainfall. In contrast, convective and mixed precipitation in the weakest rain rates occur frequently and account for 25% of the total volumetric rainfall. Stratiform precipitation as identified by ECCO only accounts for 4% of the total volumetric rainfall across all rainfall types and intensities. Over 45% of the rainfall comes from convective precipitation in the 10–25 and 25–50 mm h^{-1} rain rate bins that account for only 6% of the raining grid points.

4. Conclusions

This study uses 6 research and operational radars to examine the relationships between dynamics and rainfall in the 2022 Mei-Yu season observed by the NSF-funded PRECIP campaign. The overarching goal of PRECIP was to simplify the complexities of heavy rainfall by examining key ingredients and processes in a moisture-rich environment. The deployment of the NSF NCAR S-Pol radar in PRECIP complemented the NCU TEAM-R and 4 operational CWA radars deployed as part of TAHOPE in northern Taiwan. Quality-controlled Doppler wind data from these radars were analyzed with SAMURAI to produce three-dimensional wind fields over the Taiwan Strait northwest of Taiwan. Polarimetric data from S-Pol were used to estimate the rainfall intensity. This unique data set covers several days over two active Mei-Yu periods, providing an opportunity to statistically quantify how dynamic variables relate to rain rate intensity in the moisture-rich subtropical environment.

Stronger cyclonic rotation on the order of 10^{-3} s^{-1} is found with increasing frequency at higher rain rates along with a systematic increase in vertical velocity with rainfall intensity that maximizes in the mid to upper troposphere, with mean values on the order of a few m s^{-1}. Low-level convergence and upper-level divergence also systematically strengthen as rain rates increase. Despite covering over 21% of raining grid points, stratiform precipitation contributes only 4% of the total rainfall accumulation. Higher rain rates are increasingly convective, though the highest rain rates greater than 50 mm h^{-1} are infrequent and contribute about the same as the stratiform ($\sim$5%) to the total rainfall. The results indicate that infrequent, moderately heavy rain rates from 10 to 50 mm h^{-1} are an important contribution to overall rainfall accumulation in the Mei-Yu front, with nearly half of the volumetric rainfall accumulation resulting from only 6% of the observed raining grid points. An additional 25% of the rainfall accumulation comes from mixed and convective precipitation at low rain rates below 5 mm h^{-1}.

The analysis herein suggests that heavy rain in the Mei-Yu front does not result from fundamentally different dynamic processes compared to ordinary rainfall, but rather that distributions of dynamic variables associated with heavy rainfall are just progressively stronger on average than in lighter rain. The radar analyses indicate that the highest rain accumulations in oceanic Mei-Yu precipitation occur preferentially in moderately strong rotating convection with rain rates between 10 and 50 mm h^{-1}, and mean meso-γ scale vertical velocity and cyclonic vorticity values around 1–3 m s^{-1} and 2×10^{-4} s^{-1}, respectively. This optimal intermediate precipitation regime is between extreme rain rates that are too infrequent and frequent light rain rates that are too low to produce higher accumulations.

Disentangling the various processes and causal relations underlying the statistical relationships between rotation and rainfall shown here requires more research. We hypothesize that the observed rotation is both an effect of stretching within convection and an indirect cause of vertical motion resulting in a two-way interaction with potential feedbacks. Based on the observed vorticity strength and the vertical profile of vertical motion, the nonlinear pressure perturbation forcing is much smaller than prior studies of supercellular convection that have intense localized rotation (Coffer & Parker, 2015; Nielsen & Schumacher, 2018). Frictional boundary layer convergence beneath the rotating clouds and isentropic uplift associated with potential vorticity anomalies aloft may be playing a role. All the aforementioned processes could theoretically occur simultaneously, but the relative magnitudes may differ based on the thermodynamic environment or storm characteristics. Recent work examining mid-latitude organized convection has shown how the surrounding environmental thermodynamics and shear affects updraft width, and thus the degree to which convective updrafts are negatively impacted by entrainment (Mulholland et al., 2021; Peters et al., 2019). Future work will examine the three-dimensional characteristics of individual updrafts and their relationships with precipitation intensity, the local shearing

19448007, 2025, 24, Downloaded from https://agupubs.onlinelibrary.wiley.com/doi/10.1029/2025GL117992, Wiley Online Library on [06/02/2026]. See the Terms and Conditions (https://onlinelibrary.wiley.com/terms-and-conditions) on Wiley Online Library for rules of use; OA articles are governed by the applicable Creative Commons License

flows, and thermodynamic environment (Cole et al., 2022; Davis & Lee, 2012). Finally, the analysis herein focused on relationships in precipitation over the ocean; future work should examine how diurnal processes, increased friction, and orographic effects change these statistical relationships over land.

By focusing on statistical relationships rather than individual convective features, the results presented herein can be used to validate and improve numerical weather prediction models with comparable grid spacings of 1 km. The quantitative values of vorticity and vertical velocity and their statistical relationships can help forecasters identify regions of potential rainfall hazards. To take advantage of the relatively high spatial resolution of the radar data, the present study focuses on meso-γ scale variations in the dynamic variables. However, Mei-Yu frontal precipitation is affected by dynamics on a wide range of scales, from the synoptic scales to subgrid-scale microphysical processes. The interactions across a range of spatial scales and trajectory analysis should be considered in future work to further improve our understanding of precipitation production in moisture-rich subtropical environments.

Conflict of Interest

The authors declare no conflicts of interest relevant to this study.

Data Availability Statement

S-Pol radar data is available through the EOL Field Catalog (NCAR/EOL S-Pol Team, 2024). Operational CWA radar data were provided by Pao-Liang Chang. TEAM-R radar data came from Yu-Chieng Liou and Wei-Yu Chang from the NCU TAHOPE team. Software packages used to quality control the radar data include LROSE (DeHart et al., 2024), Py-ART (Helmus & Collis, 2016), and processorCorrect (Alford et al., 2022). Key variables from the SAMURAI analyses, along with ancillary data, are available in an online repository (DeHart & Bell, 2025).

Acknowledgments
This research was supported by National Science Foundation Grants AGS-1854559 and AGS-2103776 and NASA Grant 800NSSC23K1306. The authors thank the NSF NCAR EOL S-Pol engineers, including Michael Dixon, Ulrike Romatschke, and John Hubbert for maintaining and quality controlling the S-Pol data. The authors would like to thank the PRECIP, TAHOPE, and TPARC-II science teams. The authors thank Addison Alford for guidance on appropriate usage of processorCorrect. Finally, the authors thank the two anonymous reviewers for their comments, which improved the manuscript.

References

Alford, A. A., Biggerstaff, M. I., Ziegler, C. L., Jorgensen, D. P., & Carrie, G. D. (2022). A method for correcting staggered Pulse Repetition Time (PRT) and dual Pulse Repetition Frequency (PRF) processor errors in research radar datasets. *Journal of Atmospheric and Oceanic Technology*, *39*(11), 1763–1780. https://doi.org/10.1175/JTECH-D-21-0176.1

Balsley, B. B., Ecklund, W. L., Carter, D. A., Riddle, A. C., & Gage, K. S. (1988). Average vertical motions in the tropical atmosphere observed by a radar wind profiler on Pohnpei (7°N latitude, 157°E longitude). *Journal of the Atmospheric Sciences*, *45*(3), 396–405. https://doi.org/10.1175/1520-0469(1988)045⟨0396:AVMITT⟩2.0.CO;2

Bell, M. M., Montgomery, M. T., & Emanuel, K. A. (2012). Air–sea enthalpy and momentum exchange at major hurricane wind speeds observed during CBLAST. *Journal of the Atmospheric Sciences*, *69*(11), 3197–3222. https://doi.org/10.1175/JAS-D-11-0276.1

Cha, T.-Y., & Bell, M. M. (2023). Three-dimensional variational multi-Doppler wind retrieval over complex terrain. *Journal of Atmospheric and Oceanic Technology*, *40*(11), 1381–1405. https://doi.org/10.1175/JTECH-D-23-0019.1

Chang, P.-L., Zhang, J., Tang, Y. S., Tang, L., Lin, P. F., Langston, C., et al. (2021). An operational multi-radar multi-sensor QPE system in Taiwan. *Bulletin of the American Meteorological Society*, *102*(3), 555–577. https://doi.org/10.1175/BAMS-D-20-0043.1

Chang, W.-Y., Lee, W.-C., & Liou, Y.-C. (2015). The kinematic and microphysical characteristics and associated precipitation efficiency of subtropical convection during SoWMEX/TiMREX. *Monthly Weather Review*, *143*, 317–340. https://doi.org/10.1175/MWR-D-14-00081.1

Chen, G. T.-J. (1983). Observational aspects of the Mei-Yu phenomenon in subtropical China. *Journal of the Meteorological Society of Japan. Series II*, *61*(2), 306–312. https://doi.org/10.2151/jmsj1965.61.2_306

Chen, Y.-L., Tu, C.-C., Hsiao, F., Chen, C.-S., Lin, P.-L., & Lin, P.-H. (2022). An overview of low-level jets (LLJs) and their roles in heavy rainfall over the Taiwan area during the early summer rainy season. *Meteorology*, *1*(1), 64–112. https://doi.org/10.3390/meteorology1010006

Chien, F.-C., & Chiu, Y.-C. (2023). Factors leading to heavy rainfall in southern Taiwan in the early Mei-Yu season of 2020. *Monthly Weather Review*, *151*(7), 1885–1908. https://doi.org/10.1175/MWR-D-22-0226.1

Cifelli, R., & Rutledge, S. A. (1998). Vertical motion, diabatic heating, and rainfall characteristics in north Australia convective systems. *Quarterly Journal of the Royal Meteorological Society*, *124*(548), 1133–1162. https://doi.org/10.1002/qj.49712454806

Coffer, B. E., & Parker, M. D. (2015). Impacts of increasing low-level shear on supercells during the early evening transition. *Monthly Weather Review*, *143*(5), 1945–1969. https://doi.org/10.1175/MWR-D-14-00328.1

Cole, A. S., Bell, M. M., & DeHart, J. C. (2022). An ensemble-based analysis of a liminal extreme rainfall event near Taiwan. *Atmosphere*, *13*(7), 1011. https://doi.org/10.3390/atmos13071011

Davis, C. A., & Lee, W. C. (2012). Mesoscale analysis of heavy rainfall episodes from SoWMEX/TiMREX. *Journal of the Atmospheric Sciences*, *69*(2), 521–537. https://doi.org/10.1175/JAS-D-11-0120.1

DeHart, J., & Bell, M. (2025). PRECIP 2022 Mei-Yu front samurai analyses, estimated rain rate, and convective-stratiform partition data [Dataset]. *Dryad*. https://doi.org/10.5061/dryad.hqbzkh1vh

DeHart, J., Dixon, M., Javornik, B., Bell, M., Cha, T.-Y., DesRosiers, A., & Lee, W.-C. (2024). nsf-lrose/lrose-releases: Lrose-jade-20230814 [Software]. *Zenodo*. https://doi.org/10.5281/zenodo.11479603

Deng, D., Davidson, N. E., Hu, L., Tory, K. J., Hankinson, M. C. N., & Gao, S. (2017). Potential vorticity perspective of vortex structure changes of tropical cyclone Bilis (2006) during a heavy rain event following landfall. *Monthly Weather Review*, *145*(5), 1875–1895. https://doi.org/10.1175/MWR-D-16-0276.1

Dixon, M. J., & Romatschke, U. (2022). Three-dimensional convective–stratiform echo-type classification and convectivity retrieval from radar reflectivity. *Journal of Atmospheric and Oceanic Technology*, *39*(11), 1685–1704. https://doi.org/10.1175/JTECH-D-22-0018.1

Dixon, M. J., Wilson, J. W., Weckwerth, T. M., Albo, D., & Thompson, E. J. (2015). A dual-polarization QPE method based on the NCAR particle ID algorithm description and preliminary results. In *37th conference on radar meteorology*. American Meteorological Society. Retrieved from https://ams.confex.com/ams/37RADAR/webprogram/Paper275705.html

Doswell, C. A., Brooks, H. E., & Maddox, R. A. (1996). Flash flood forecasting: An ingredients-based methodology. *Weather and Forecasting*, *11*, 560–581. https://doi.org/10.1175/1520-0434(1996)011⟨0560:FFFAIB⟩2.0.CO;2

Eliassen, A., & Lystad, M. (1977). The Ekman layer of a circular vortex: A numerical and theoretical study. *Geophysica Norvegica*, *31*, 1–16.

Helmus, J. J., & Collis, S. M. (2016). The python ARM radar toolkit (Py-ART), a library for working with weather radar data in the python programming language. *Journal of Open Research Software*, *4*(1), 25. https://doi.org/10.5334/jors.119

Houze, R. A. (1989). Observed structure of mesoscale convective systems and implications for large-scale heating. *Quarterly Journal of the Royal Meteorological Society*, *115*(487), 425–461. https://doi.org/10.1002/qj.49711548702

Ke, C. Y., Chung, K. S., Wang, T. C. C., & Liou, Y. C. (2019). Analysis of heavy rainfall and barrier-jet evolution during Mei-Yu season using multiple Doppler radar retrievals: A case study on 11 June 2012. *Tellus, Series A: Dynamic Meteorology and Oceanography*, *71*, 1–21. https://doi.org/10.1080/16000870.2019.1571369

Klemp, J. B. (1987). Dynamics of tornadic thunderstorms. *Annual Review of Fluid Mechanics*, *19*(1), 369–402. https://doi.org/10.1146/annurev.fl.19.010187.002101

Lai, H. W., Davis, C. A., & Jou, B. J. D. (2011). A subtropical oceanic mesoscale convective vortex observed during SoWMEX/TiMREX. *Monthly Weather Review*, *139*(8), 2367–2385. https://doi.org/10.1175/2010MWR3411.1

Marinescu, P. J., Kennedy, P. C., Bell, M. M., Drager, A. J., Grant, L. D., Freeman, S. W., & van den Heever, S. C. (2020). Updraft vertical velocity observations and uncertainties in high plains supercells using radiosondes and radars. *Monthly Weather Review*, *148*(11), 4435–4452. https://doi.org/10.1175/MWR-D-20-0071.1

Mazurek, A. C., & Schumacher, R. S. (2023). Quantifying the relationship between embedded rotation and extreme rainfall rates in observations of tropical storm Imelda (2019). *Monthly Weather Review*, *151*(5), 1109–1128. https://doi.org/10.1175/MWR-D-22-0115.1

Mulholland, J. P., Peters, J. M., & Morrison, H. (2021). How does LCL height influence deep convective updraft width? *Geophysical Research Letters*, *48*(13), e2021GL093316. https://doi.org/10.1029/2021GL093316

NCAR/EOL S-Pol Team. (2024). PRECIP: NCAR S-Pol radar moments data. Version 2.0 [Dataset]. *UCAR/NCAR - Earth Observing Laboratory*. https://doi.org/10.26023/QA4M-CDHH-MY0Z

Nielsen, E. R., & Schumacher, R. S. (2018). Dynamical insights into extreme short-term precipitation associated with supercells and mesovortices. *Journal of the Atmospheric Sciences*, *75*(9), 2983–3009. https://doi.org/10.1175/JAS-D-17-0385.1

Ninomiya, K., & Murakami, T. (1987). The early summer rainy season (Baiu) over Japan. In C.-P. Chang & T. N. Krishnamurti (Eds.), *Monsoon meteorology* (pp. 93–121). Oxford Univ. Press.

Oye, R., Mueller, C., & Smith, S. (1995). Software for radar translation, visualization, editing, and interpolation. In *27th conf. on radar meteorology*. American Meteorological Society.

Paul, S., Wang, C., Chien, F., & Lee, D. (2018). An evaluation of the WRF Mei-Yu rainfall forecasts in Taiwan, 2008–2010: Differences in elevation and sub-regions. *Meteorological Applications*, *25*(2), 269–282. https://doi.org/10.1002/met.1689

Peters, J. M., Nowotarski, C. J., & Morrison, H. (2019). The role of vertical wind shear in modulating maximum supercell updraft velocities. *Journal of the Atmospheric Sciences*, *76*(10), 3169–3189. https://doi.org/10.1175/JAS-D-19-0096.1

Raymond, D. J., & Jiang, H. (1990). A theory for long-lived mesoscale convective systems. *Journal of the Atmospheric Sciences*, *47*(24), 3067–3077. https://doi.org/10.1175/1520-0469(1990)047⟨3067:ATFLLM⟩2.0.CO;2

Rotunno, R., & Klemp, J. B. (1982). The influence of the shear-induced pressure gradient on thunderstorm motion. *Monthly Weather Review*, *110*(2), 136–151. https://doi.org/10.1175/1520-0493(1982)110⟨0136:TIOTSI⟩2.0.CO;2

Schumacher, C., Stevenson, S. N., & Williams, C. R. (2015). Vertical motions of the tropical convective cloud spectrum over Darwin, Australia. *Quarterly Journal of the Royal Meteorological Society*, *141*(691), 2277–2288. https://doi.org/10.1002/qj.2520

Tao, S., & Chen, L. (1987). A review of recent research on East Asian summer monsoon in China. In *Monsoon meteorology* (pp. 60–92). Oxford Univ. Press.

Trier, S. B., Davis, C. A., & Tuttle, J. D. (2000). Long-lived mesoconvective vortices and their environment. Part I: Observations from the central United States during the 1998 warm season. *Monthly Weather Review*, *128*(10), 3376–3395. https://doi.org/10.1175/1520-0493(2000)128⟨3376:LLMVAT⟩2.0.CO;2

Ulanski, S. L., & Garstang, M. (1978). The role of surface divergence and vorticity in the life cycle of convective rainfall. Part I: Observation and analysis. *Journal of the Atmospheric Sciences*, *35*, 1047–1062. https://doi.org/10.1175/1520-0469(1978)035⟨1047:TROSDA⟩2.0.CO;2

Vivekanandan, J., Ellis, S. M., Oye, R., Zrnic, D. S., Ryzhkov, A. V., & Straka, J. (1999). Cloud microphysics retrieval using S-band dual-polarization radar measurements. *Bulletin of the American Meteorological Society*, *80*(3), 381–388. https://doi.org/10.1175/1520-0477(1999)080⟨0381:CMRUSB⟩2.0.CO;2

Wang, C.-C., Chuang, P.-Y., Chang, C.-S., Tsuboki, K., Huang, S.-Y., & Leu, G.-C. (2022). Evaluation of Mei-Yu heavy-rainfall quantitative precipitation forecasts in Taiwan by a cloud-resolving model for three seasons of 2012–2014. *Natural Hazards and Earth System Sciences*, *22*(1), 23–40. https://doi.org/10.5194/nhess-22-23-2022

Wang, C.-C., Li, M.-S., Chang, C.-S., Chuang, P.-Y., Chen, S.-H., & Tsuboki, K. (2021). Ensemble-based sensitivity analysis and predictability of an extreme rainfall event over northern Taiwan in the Mei-Yu season: The 2 June 2017 case. *Atmospheric Research*, *259*, 105684. https://doi.org/10.1016/j.atmosres.2021.105684

Xu, W., Zipser, E. J., & Liu, C. (2009). Rainfall characteristics and convective properties of Mei-Yu precipitation systems over South China, Taiwan, and the South China Sea. Part I: TRMM observations. *Monthly Weather Review*, *137*(12), 4261–4275. https://doi.org/10.1175/2009MWR2982.1

Zhou, H. (2009). Study on the mesoscale structure of the heavy rainfall on Mei-Yu front with dual-Doppler radar. *Atmospheric Research*, *93*(1–3), 335–357. https://doi.org/10.1016/j.atmosres.2008.10.011

References From the Supporting Information

Collaboration, T. A., Price-Whelan, A. M., Lim, P. L., Earl, N., Starkman, N., Bradley, L., et al. (2022). The Astropy project: Sustaining and growing a community-oriented open-source project and the latest major release (v5.0) of the core package. *The Astrophysical Journal*, *935*(2), 167. https://doi.org/10.3847/1538-4357/ac7c74

19448007, 2025, 24, Downloaded from https://agupubs.onlinelibrary.wiley.com/doi/10.1029/2025GL117992, Wiley Online Library on [06/02/2026]. See the Terms and Conditions (https://onlinelibrary.wiley.com/terms-and-conditions) on Wiley Online Library for rules of use; OA articles are governed by the applicable Creative Commons License

NASA JPL. (2013). NASA shuttle radar topography mission global 1 arc second [Dataset]. *NASA EOSDIS Land Processes Distributed Active Archive Center*. https://doi.org/10.5067/MEaSUREs/SRTM/SRTMGL1.003

Price-Whelan, A. M., Sipőcz, B. M., Günther, H. M., Lim, P. L., Crawford, S. M., Conseil, S., et al. (2018). The Astropy project: Building an open-science project and status of the v2.0 core package. *The Astronomical Journal*, *156*(3), 123. https://doi.org/10.3847/1538-3881/aabc4f

Robitaille, T. P., Tollerud, E. J., Greenfield, P., Droettboom, M., Bray, E., Aldcroft, T., et al. (2013). Astropy: A community python package for astronomy. *Astronomy & Astrophysics*, *558*, A33. https://doi.org/10.1051/0004-6361/201322068

Virtanen, P., Gommers, R., Oliphant, T. E., Haberland, M., Reddy, T., Cournapeau, D., et al. (2020). SciPy 1.0: Fundamental algorithms for scientific computing in python. *Nature Methods*, *17*(3), 261–272. https://doi.org/10.1038/s41592-019-0686-2

19448007, 2025, 24, Downloaded from https://agupubs.onlinelibrary.wiley.com/doi/10.1029/2025GL117992, Wiley Online Library on [06/02/2026]. See the Terms and Conditions (https://onlinelibrary.wiley.com/terms-and-conditions) on Wiley Online Library for rules of use; OA articles are governed by the applicable Creative Commons License